Journal of Alloys and Compounds 1043 (2025) 184136

Contents lists available at ScienceDirect

Journal of Alloys and Compounds

journal homepage: www.elsevier.com/locate/jalcom

Investigating crystallisation kinetics of $Fe_{40}Ni_{40}P_{14}B_6$ and $Fe_{40}Ni_{40}B_{20}$ metallic glasses using simultaneous time-resolved quick-EXAFS and XRD

Sebastian Paripsa [a,*], Abhijeet Gaur [b], Dirk Lützenkirchen-Hecht [a]

[a] Fk. 4, Physik, Bergische Universität Wuppertal, Gaußstraße 20, Wuppertal D-42097, Germany
[b] Institute for Chemical Technology and Polymer Chemistry, Karlsruhe Institute of Technology, Engesserstraße 20, Karlsruhe D-76131, Germany

ARTICLE INFO

Keywords:
Amorphous alloys
Crystallisation kinetics
In-situ investigation
X-ray absorption spectroscopy
X-ray diffraction
Fe-Ni based metallic glasses
Debye-Waller factor

ABSTRACT

This study employs in-situ multi-edge quick-EXAFS and XRD to resolve the crystallisation kinetics of $Fe_{40}Ni_{40}P_{14}B_6$ and $Fe_{40}Ni_{40}B_{20}$ metallic glasses for different heating programs. Time-resolved analysis reveals that $Fe_{40}Ni_{40}P_{14}B_6$ crystallises via preferential Ni_3P/γ-Fe formation with quick medium-to long-range ordering, while $Fe_{40}Ni_{40}B_{20}$ follows a slower $(Fe,Ni)_3B/\gamma$-FeNi route. Metal-metalloid bonds (Fe-P/Ni-P, Fe-B/Ni-B) exhibit decreasing Debye-Waller factors (σ^2) during nucleation, signalling local ordering, while metal-metal bonds (Fe-Fe/Ni-Ni) show mostly increasing σ^2 due to bond tightness and compositional fluctuations. Heating rates (0.25–2.08 K/s) critically influence the crystallisation onset temperatures (684–867 K), with faster rates delaying the nucleation but preserving phase identity. This work establishes a methodology for correlating short/long-range order dynamics in glass-crystal transitions.

1. Introduction

A combination of mechanical strength, soft-magnetic behaviour and corrosion resistance has made amorphous metallic alloys (metallic glasses) attractive candidates for functional materials, advanced coatings, transformer cores and biomagnetic field sensors since the 1960s [1–6]. While many compositions exist, Fe-based metallic glasses, such as $Fe_{40}Ni_{40}P_{14}B_6$ (commercial name: Metglas 2826) and $Fe_{40}Ni_{40}B_{20}$ have use in production, industrial and medical applications due to high hardness, soft magnetic behaviour, relatively low cost and its ability to retain an amorphous state over a relatively wide temperature range [3,7,8]. Composition selection allows property tuning: while the transition metal Ni enhances the thermal stability against crystallisation and supplements the iron-dominated matrices (40 %Fe) by the fcc-stabilising effects (face-centred cubic), the glass-forming elements (B, P) improve and help forming a fully amorphous structure by disrupting the lattice and inhibiting nucleation sites [3,9].

The thermal stability and crystallisation behaviour of these alloys remain areas of active research. Upon heating, crystallisation begins at an onset temperature T_{onset}, evidenced by the first appearance of Bragg reflections (and an associated calorimetric exotherm), after which the microstructure evolves by nucleation and growth [6,10–12]. Both alloys therefore undergo significant structural transformations when heated, transitioning from a disordered atomic arrangement to (quasi)crystalline phases [7,13–21]. To resolve the underlying atomic structure, complementary characterisation techniques covering both long-range and short-range order are useful due to the differences in crystalline and amorphous systems. Therefore, a combined approach of X-ray absorption spectroscopy (XAS) [22] and X-ray diffraction (XRD) [23] is beneficial in studying $Fe_{40}Ni_{40}P_{14}B_6$ and $Fe_{40}Ni_{40}B_{20}$ metallic glasses under thermal treatment. XRD detects long-range periodicity (sharp peaks) alongside amorphous halos [24], whereas XAS (extended X-ray absorption fine structure (EXAFS) and X-ray absorption near-edge structure (XANES)) provides element specific short-range information, namely coordination numbers, bond lengths and disorder (Debye-Waller) parameters, in both disordered and partially ordered states [25,26]. In time-resolved experiments, XRD tracks long-range structural change and crystallisation kinetics, while quick-EXAFS (QEXAFS) follows the time- and temperature-dependent evolution of local coordination. Combined, these techniques give insights about the amorphous-to-crystalline pathway, which is relevant for amorphous Fe-Ni-P/B alloys, where controlling short-range rearrangements controls long-range crystallisation and hence the functional behaviour. The present work determines the kinetics of the amorphous-crystalline transition in $Fe_{40}Ni_{40}P_{14}B_6$ and $Fe_{40}Ni_{40}B_{20}$ alloys, using simultaneous time-resolved QEXAFS and XRD [27].

* Corresponding author.
E-mail address: paripsa@uni-wuppertal.de (S. Paripsa).

https://doi.org/10.1016/j.jallcom.2025.184136
Received 18 July 2025; Received in revised form 15 September 2025; Accepted 29 September 2025
Available online 30 September 2025

2. Materials and methods

The $Fe_{40}Ni_{40}P_{14}B_6$ ribbon foils were produced by melt spinning and underwent electrolytic etching in aqueous hydrochloric acid (HCl) to remove surface impurities and oxidation layers. Each sample was polished with a 1 μm abrasive to ensure a uniform and smooth surface suitable for X-ray transmission. All $Fe_{40}Ni_{40}B_{20}$ samples were produced by vacuum melting to maintain the alloy's purity and amorphous structure and then underwent similar etching and polishing procedures. Foil samples (≈7–15 μm thick) were assigned unique identifiers and secured at both ends within a custom copper sample holder featuring a central aperture for X-ray transmission (Fig. S1). The holder was mounted centrally inside the in-situ cell (dome) of the Anton Paar DHS 1100 [28] with controller TCU 200 and fastened using spring-loaded clamps provided with the dome. This equipment is regularly available at several synchrotron sources (e.g. PETRA III, DESY, Germany, and Photon Factory, KEK, Japan) and has been frequently used for in-situ X-ray investigations at elevated temperatures [29–33]. Before data acquisition, the system was evacuated with a backing pump to a vacuum of approximately 10^{-2} mbar. Under these controlled conditions, QEXAFS and XRD measurements were done simultaneously, while the corresponding temperature profile was recorded continuously. For each sample, a distinct heating ramp (annealing) and an isothermal annealing phase was applied (Table 1) to systematically understand the thermal evolution and kinetics of phase transformations - crystallisation and relaxation processes - within the material. Temperature measurement in the dome does not happen directly at the sample surface, but by using a thermocouple embedded in the heating plate. Thus, heat transfer occurs through limited conduction and radiation, which creates temperature offsets between displayed (heater plate) and actual (foil) temperatures.

Quick-scanning EXAFS and XRD measurements were conducted in-situ at the QEXAFS beamline P64 at PETRA III (DESY, Hamburg, Germany, [34–36]). For diffraction, an incident X-ray energy of 6.998 keV was selected using a Si(111) monochromator, and scattered intensities were processed with a PILATUS 100k pixel detector (Dectris, Dübendorf, Switzerland). XAS spectra were continuously acquired in transmission, simultaneously for both the Fe K-edge (7.112 keV) and Ni K-edge (8.333 keV) while samples were heated in-situ (previous section). The starting Bragg angle of the Si(111) monochromator was set to Θ≈ 14.8°, satisfying Bragg's law for an X-ray energy of ≈ 7.7 keV, which lies midway between the Fe- and Ni K-edge. From that position the monochromator was driven by a sinusoidal motion ±ΔΘ during each QEXAFS swing, yielding an energy sweep from ≈ 7.0–9.0 keV and thus, covering both absorption edges in a single continuous scan.

QEXAFS spectra were measured at 0.25 Hz; each complete EXAFS scan captured one full spectrum (up and down) at both the Fe- and the Ni K-absorption edges of the samples every 4 s. While rapid changes in the sample might be averaged out a bit at this scan speed, the benefit is an improved signal quality required for this sensitive samples, due to longer integration time. For frame-accurate pairing of XRD and EXAFS, one diffraction image must be recorded for each EXAFS spectrum at a defined photon energy; in QEXAFS mode, the monochromator crystal moves continuously in a sinusoidal pattern, so the beam energy is always changing. In the combined setup for this work however, a signal of the third harmonic wave with a fitting amplitude is added to the sinusoidal drive signal that moves the monochromator [34–36]. This flattens the turning points (minima/maxima) to create short energy plateaus. This ensures that the XRD patterns were recorded simultaneously with the QEXAFS scans during the thermal treatment. Hence, changes in local atomic structure (short-range to mid-range order from EXAFS) can be directly correlated with phase transformations observed by diffraction at the same time (long-range order).

Table 1
Used samples, chosen temperature programs for each measurement, and T_{onset} of crystallisation for the chosen temperature programs. SPR = set point (heating) rate.

Sample	Sample ID	SPR (K/s)	T_{end} (K)	Isothermal annealing	T_{onset} (K)
$Fe_{40}Ni_{40}P_{14}B_6$	ID9_1	0.25	872	872 K for 34 min	(684 +/- 5)
	ID4_2	0.50	1013		(690 +/- 5)
	ID4_1	0.67	1013	1013 K for 34 min 1013 K for 32 min	(707 +/- 5)
	ID18_1	1.67	872	872 K for 30 min	(717 +/- 10)
$Fe_{40}Ni_{40}B_{20}$	ID13_2 (only XAS)	0.25	872	872 K for 32 min	-
		1.67	872		(825 +0/- 50)
	ID13_1	2.08	872	872 K for 41 min	
	ID14_2 (only XRD)			872 K for 30 min	(867 +0/- 50)

The acquired temperature data was calibrated against the known melting temperature of lead-free solder (T ≈ 500 K) using similar in-situ conditions with the same AP DHS 1100, which ensured an accurate sample temperature determination. Each measured raw spectrum was processed to get normalized absorbance μ(E), converted into k-space (k^3-weighted EXAFS fine structures $\chi(k)*k^3$) and into R-space (FT[$\chi(k)*k^3$] of the k^3-weighted EXAFS) using Athena [37]. To ensure consistency, to all spectra from one heating rate the same Fourier window was applied. More details about the data treatment are compiled in the **supplementary section S3**. Artemis (version 0.8.012) [37] was employed for EXAFS fitting with crystallographic data of Fe_3P [38], Ni_3P [39], Fe_3B [40], Ni_3B [41]. The specific set of utilised paths and parameter constraints are detailed in the next section. Fit results (parameters with uncertainties) were exported and further processed with a custom Python script (example: https://github.com/San-WierPa/artemis-fit-formatter and **section S7)**. Fit parameters are reported as: N - coordination number, R - bond distance (Å), σ^2 - DW factor ($Å^2$), and R-factor - goodness of fit. Error bars are given in parentheses. *t* denotes the time of isothermal annealing (min) measured from the start of the isothermal hold. Temperature uncertainties are: for $Fe_{40}Ni_{40}P_{14}B_6$ datasets up to T = 1013 K, ±50 K for T ≥ 985 K and ±30 K for T < 985 K; for datasets up to T = 872 K, ±50 K for T ≥ 827 K and ±30 K for T < 827 K; for $Fe_{40}Ni_{40}B_{20}$, ±50 K for all runs. These temperature uncertainties apply uniformly across all relevant tables.

For the 2D X-ray diffraction images (.tif; Fig. 1 for exemplary results) which were collected during the in-situ experiments, the PyFAI library (Python toolkit for calibration and fast azimuthal integration) has been used [42]; details are in **section S2**. Five temperature sections were selected: 1) pristine amorphous; 2) onset of crystallisation (first Bragg reflections); 3) early crystalline growth; 4) pre-relaxation; 5) structural relaxation after isothermal annealing. Diffraction patterns are plotted in Python, together with lightly smoothed intensity curves using a Savitsky-Golay filter for clearer visualisation of trends. All phase identification and analysis, however, were performed on the unsmoothed integrated data. Using this workflow, we obtained a comprehensive set of synchronised EXAFS and XRD data that capture the structural evolution of the Fe–Ni–P/B alloys during heating and isothermal annealing. The following section presents these results.

3. Results and discussion

3.1. In-situ XRD

Table 1 and Fig. 2 offer an overview of the onset of crystallisation temperature T_{onset} for both materials and the different heating ramps. $Fe_{40}Ni_{40}P_{14}B_6$ shows a lower T_{onset} compared to $Fe_{40}Ni_{40}B_{20}$ which showed greater variations in the data, and for which we report correspondingly larger uncertainties. Overall, T_{onset} increases with heating rate, due to the kinetic delay of nucleation, which is in perfect agreement with prior findings for $Fe_{40}Ni_{40}P_{14}B_6$ [13] and, considering the

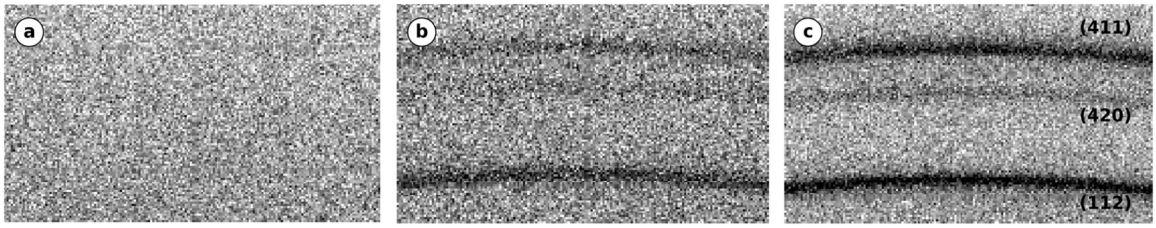

Fig. 1. Selected 2D diffraction frames of $Fe_{40}Ni_{40}P_{14}B_6$ recorded in-situ during the 0.67 K/s ramp. (a) Pristine amorphous foil at T = 300 K: the pattern shows only diffuse scattering; no Debye–Scherrer rings are visible. (b) Intermediate stage (T ≈ 707 K): three more or less faint, continuous rings appear, marking the first nucleation of crystalline domains, i.e. onset of crystallisation. (c) Fully crystallised state (T = 1013 K): bright, sharp Debye–Scherrer rings corresponding to the (112), (420) and (411) reflections of tetragonal Ni_3P confirm long-range ordering and grain growth.

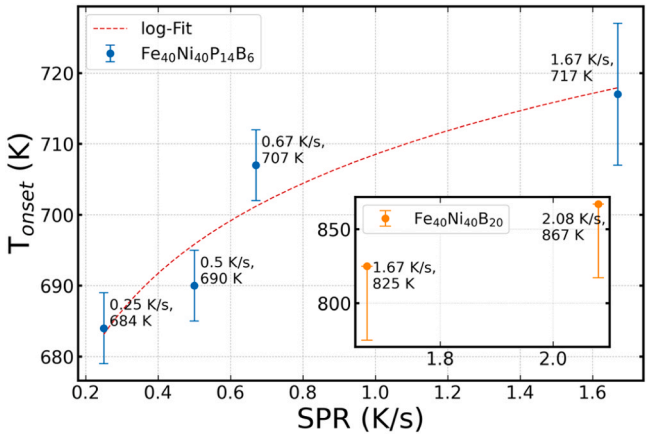

Fig. 2. Dependence of crystallisation onset temperature T_{onset} versus the heating rate SPR for the two analysed metallic alloys. Blue dots show T_{onset} for $Fe_{40}Ni_{40}P_{14}B_6$ with error bars (Table 1). The red dashed curve is a logarithmic fit. The inset displays $Fe_{40}Ni_{40}B_{20}$ data with corresponding error bars.

greater variation, in good agreement for $Fe_{40}Ni_{40}B_{20}$ [19]. An additional Kissinger analysis of the crystallisation onsets yields an effective activation energy $E_{a,eff}$= 188 + /- 48 kJ/mol for $Fe_{40}Ni_{40}P_{14}B_6$, consistent with Fe-based metallic glasses (≈200–300 kJ/mol under comparable conditions; higher values often arise from DSC peak temperatures or different crystallisation stages). For $Fe_{40}Ni_{40}B_{20}$ only two rates were available, yielding an estimate of ≈ 18 kJ/mol; which we report without further interpretation.

Based on previous studies [13,19] and complementary PowderCell [43] simulations, the expected crystallisation products are for $Fe_{40}Ni_{40}P_{14}B_6$ the tetragonal Ni_3P phase together with γ-Fe (face--centred cubic, fcc) and for the $Fe_{40}Ni_{40}B_{20}$ an orthorhombic $(Fe,Ni)_3B$ together with γ-FeNi (face-centred cubic, fcc). For peak indexing we use prototype structures as references: Ni_3P has a tetragonal I-4 structure (space group 82, a=b=8.954 Å, c=4.386 Å, α=β=γ=90°), γ-Fe has a face-centred cubic F4/m-32/m structure (space group 225, a=b=c=3.567 Å, α=β=γ=90°), Fe_3Ni_3B has an orthorhombic Pnma structure (space group 62, a=5.44 Å, b=6.65 Å, c=4.46 Å for Ni_3B, a=5.223 Å, b=6.615 Å, c=4.392 Å for Fe_3B, α=β=γ=90° for both), and fcc Fe-Ni has a tetragonal P4/m2/m2/m structure (space group 123, a=b=2.531 Å, c=3.58 Å, α=β=γ=90°). The simulated diffraction patterns for these phases align well with the observed XRD peaks, and thus, providing a credible basis for interpreting not only the in-situ diffraction data, but also for the analysis of the in-situ QEXAFS data. The XRD patterns in **Figs. 3** and **S2-S3** track the transformation from the amorphous state to a crystalline state under the heating programs.

In the diffraction profiles, the pristine amorphous state exhibits a broad diffuse halo with no sharp Bragg peaks (sub-panels (e) and (j) in **Figs. 3** and **S2-S3**), except for a broad peak near 2Θ≈ 61° that persists in the amorphous regime and is assigned to the second diffuse maximum characteristic of metallic glasses; no discrete Bragg reflections are observed in the pristine state. Upon heating, distinct diffraction peaks emerge at specific 2Θ positions corresponding to the Ni_3P, (most prominently the (112)-reflection at 2Θ= 50.5° and the (411)-peak at 2Θ= 54.5°) respectively the $(Fe,Ni)_3B$ intermetallic phases ((031)-diffraction at 2Θ= 53°) and the γ-FeNi phase ((200)-peak at 2Θ= 57°), marking the onset and subsequent progression of crystallisation.

Once nucleation begins, the diffraction patterns transition cleanly from a diffuse halo to discrete Bragg reflections, allowing phase identification. Broad features gradually resolve into well-defined peaks whose intensities increase with time and temperature. Notably, once the first peak(s) are visible, a significant growth in intensity happens quickly; e.g. the peak at 2Θ≈ 50.5° of Ni_3P (112) reflection in Fig. 3-**left** rises from 3 a.u. at the onset (d) to 7 a.u. in the next state (c) over ΔT = 11 K. At the peak annealing temperatures (T = 1013 K, respectively T = 872 K), the dominant reflexions are established and sharpen, signalling substantial crystallite growth. The emergence and late sharpening of higher-angle peaks emphasise the development of long-range order. Most prominent is the small-angle amorphous hump in $Fe_{40}Ni_{40}B_{20}$ (Fig. 3-**right**), which transforms into a distinct peak, indexed as Ni_3B (121). This sharpening of peaks is consistent with the inverse peak-width-size relation (Scherrer) [44,45]: corresponding crystallite sizes are listed in **section S8**.

For a given phase, positions of the main diffraction peaks remain essentially constant across heating rates, indicating that the same phase composition and lattice parameters are obtained under both slow and fast heating conditions. During the isothermal annealing at maximum temperature, the existing diffraction patterns become more intense and slightly narrower, consistent with structural relaxation (coarsening and/or reduced microstrain). Most importantly, no new peaks appear during the hold, so phase identification is complete at this point. This confirms that crystallisation is fully completed before any cooling phase occurs. After sustained annealing (or subsequent cooling) we observed a modest shift to higher 2Θ values (smaller d-spacings) for all peak positions. This is due to structural relaxation at temperature and thermal contraction on cooling, not to new phase formation. The absence of additional rings/peaks through the isothermal annealing or cooling verifies that no further transformations occur beyond the initial formation of Ni_3P + γ-Fe or $(Fe,Ni)_3B$ + γ-(Fe,Ni); accordingly, we did not analyse the cooling phase further.

At heating rates 1.67 K/s (Fig. S2-**right)** and 2.08 K/s (Fig. S3-**left)** several late-forming reflections are weaker or absent, compared with slower ramps. This is compatible with limited growth time at high rates and/or persistent broadening from small crystallites (overlap of weak peaks). Thus, the essential phases set forms, but aspects of the final coarsening are truncated by kinetics. In summary, XRD confirms the anticipated pathways - Ni_3P + γ-Fe, respectively $(Fe,Ni)_3B$ + γ-FeNi - and resolves key features such as crystallisation onset temperatures, crystallite growth due to peak sharpening, and phase stability across heating programs.

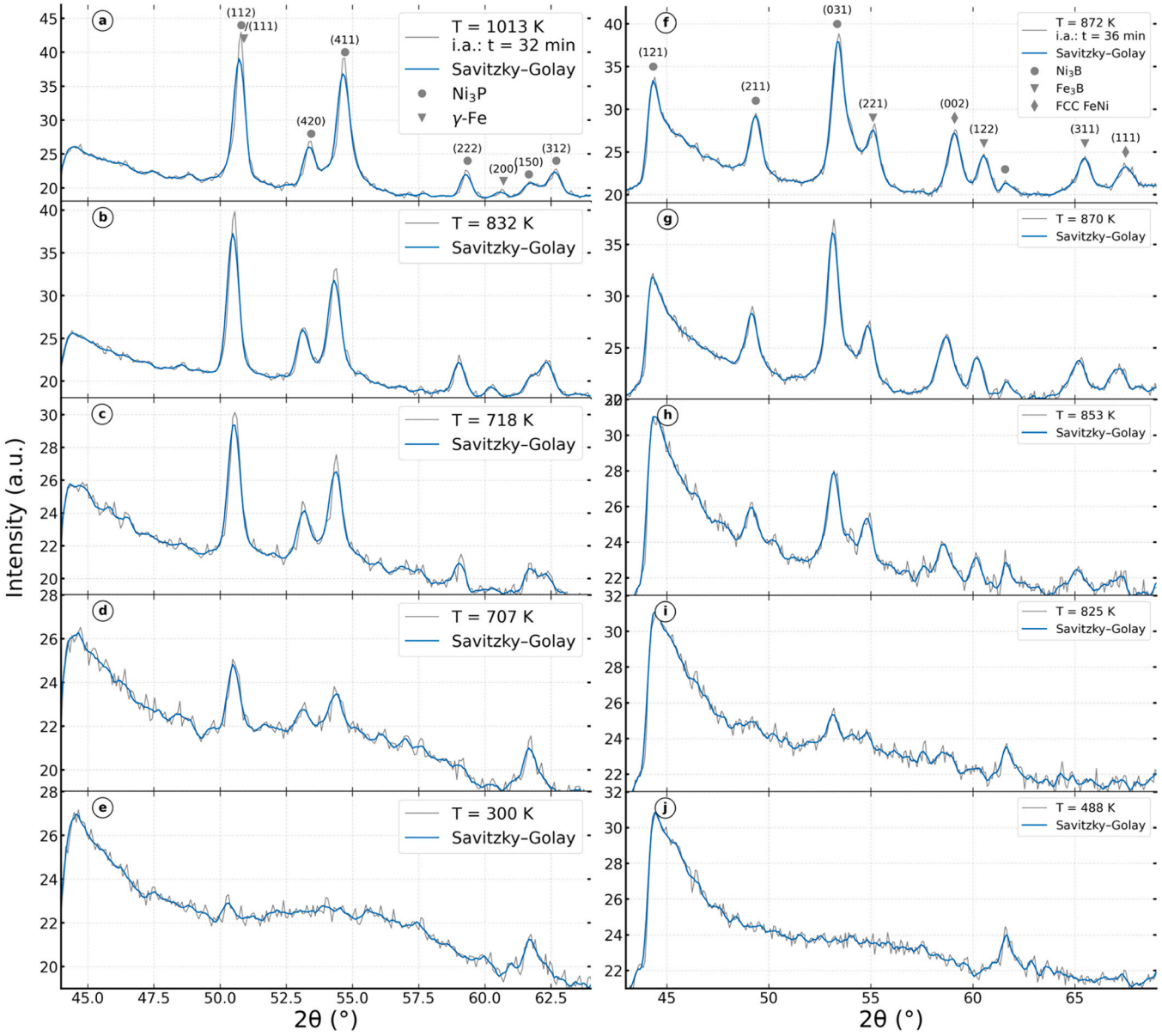

Fig. 3. Diffraction evolution calculated by azimuthal integration of $Fe_{40}Ni_{40}P_{14}B_6$ at a heating process of 0.67 K/s ((a)-(e)) and of $Fe_{40}Ni_{40}B_{20}$ at a heating process 1.67 K/s ((f)-(j)) for different temperatures – annealing (e)-(b), (j)-(g) and after isothermal annealing (i.a.) (a), (f). The pristine amorphous state is in (e) and (j), the onset of crystallisation at T = (707 +/- 5) K in (d) and at T = (825 +0/- 50) K in (i), further crystallisation in (c), (b) and (h), (g), and after structural relaxation with a slight right shift of the peaks in (a) and (f).

3.2. In situ QEXAFS

This section presents the time-resolved XAS analysis of the amorphous-to-crystalline transformation in $Fe_{40}Ni_{40}P_{14}B_6$ and $Fe_{40}Ni_{40}B_{20}$ foils, performed during controlled heating ramps (annealing + isothermal annealing). Using Fe- and Ni K-edge QEXAFS data, element-specific re-ordering of the nearest neighbour environments is tracked and correlated with changes in simultaneous XRD and the corresponding temperature profiles (Table 1). In the amorphous matrices only nearest-neighbour distances are well defined; upon crystallisation, additional, narrower peaks emerge at larger R-values. The results of quantitative EXAFS fitting - bond distances and Debye Waller (DW) factors as a function of temperature and heating rate - are further discussed.

Normalized Fe/Ni K-edge XANES evolution of $Fe_{40}Ni_{40}P_{14}B_6$ for the four heating rates are displayed in Fig. 4 and **S4**. For reference, normalized pristine Fe and Ni foil data (measured at P64; to be uploaded to *RefXAS* - http://xafsdb.ddns.net/) are plotted. All spectra super-pose smoothly across the different ramp rates and temperatures. Between ≈ 7.11–7.12 keV, respectively between ≈ 8.33–8.34 keV the curves collapse into a narrow band. The k^3-weighted EXAFS ($\chi(k)*k^3$ vs k) in **Figs. 5** and **S4** show a systematic amplitude increase with temperature, consistent with reduced local disorder and growing order during crystallisation. This trend is more pronounced for the region k ≈ 4–8 $Å^{-1}$ and mirrors the sharpening of each of the corresponding peaks in the FT [$\chi(k)*k^3$] (**Figs. 6** and **S5**). In the post-edge regions - ≈ 7.13–7.14 keV (Fe), respectively ≈ 8.35–8.36 keV (Ni) - low-temperature spectra (see colour code) are concave-down, whereas the spectra recorded above the onset of crystallisation

(≈700 K) become concave-up. The upper-right insets in Fig. 4 and **S4**) highlight this inversion with an upwards pointing arrow. This change is consistent across all four heating ramps at both edges, indicating a structural transition rather than thermal expansion. Quantitatively, the increasing normalised absorbance marks the concavity flip

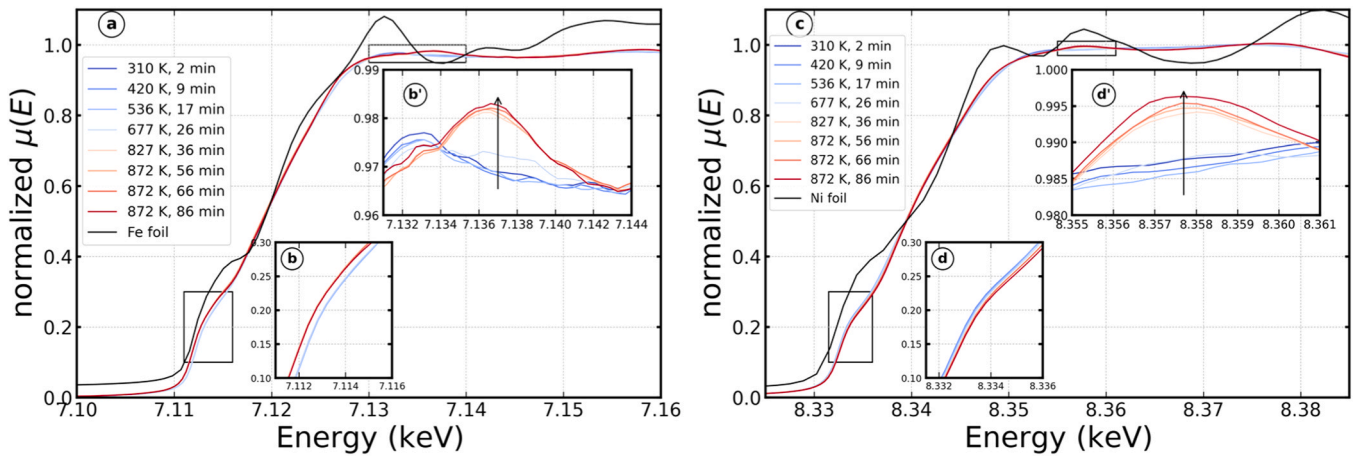

Fig. 4. Time-resolved X-ray absorption near-edge spectra (XANES) (a, c) measured at the Fe- and Ni K-edges during exposure of $Fe_{40}Ni_{40}P_{14}B_6$ at a heating rate of 0.25 K/s. The colour code goes from blue to dark orange with increasing temperature and isothermal annealing time for T = (872 +/- 30) K. Insets ((b, b'), (d, d')) show the responding zoomed out regions of the edge region (lower boxes) and the post-white line region (upper boxes). Additionally, (a) and (c) show the normalized XANES of pristine Fe- and Ni foil for comparison. Full panel set provided in Fig. S4.

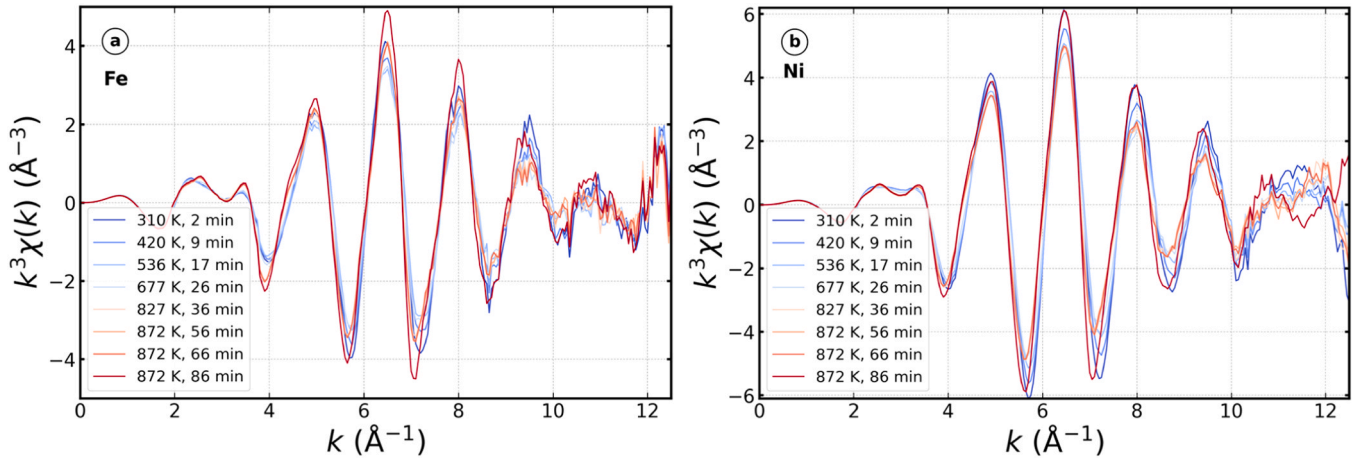

Fig. 5. k^3-weighted χ(k) spectra at the Fe- and Ni K-edges during exposure of $Fe_{40}Ni_{40}P_{14}B_6$ at a heating rate of 0.25 K/s. Full panel set provided in Fig. S4.

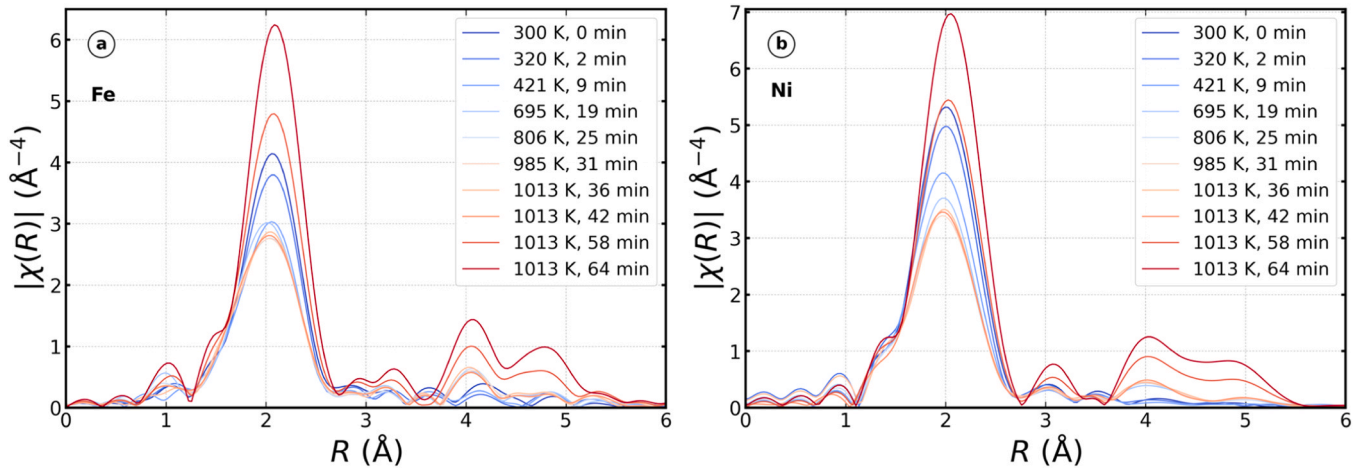

Fig. 6. Magnitude of the Fourier transform of the k^3-weighted EXAFS at the Fe- and Ni K-edges during exposure of $Fe_{40}Ni_{40}P_{14}B_6$ at a heating rate of 0.50 K/s. Sequential appearance of new shells between R≈ 3 Å and R≈ 5 Å trace the transition from amorphous to crystalline. Final positions of the shells are identical; hence, they originate from long-range ordering. Full panel set provided in Fig. S5.

from the low-temperature curves (blue) to the high-temperature curves (dark orange) for the Fe K-edge by $\Delta\mu \approx 0.016$ (0.25 K/s), $\Delta\mu \approx 0.013$ (0.50 K/s), $\Delta\mu \approx 0.015$ (0.67 K/s), and $\Delta\mu \approx 0.011$ (1.67 K/s). For the Ni K-edge by $\Delta\mu \approx 0.012$ (0.25 K/s), $\Delta\mu \approx 0.010$ (0.50 K/s), $\Delta\mu \approx 0.015$ (0.67 K/s), and $\Delta\mu \approx 0.011$ (1.67 K/s). Thus, Fe shows a slightly larger inversion at the slower ramps, consistent with Fe-centred order maturing earlier; at faster ramps the Fe and Ni amplitudes converge. The full panel set is provided in Fig. S4-S5; the main text retains one representative panel for both Fe and Ni to illustrate the effect. Multiple-scattering calculations for Fe–P/B glasses show such a phase reversal when Fe–Fe or Ni-Ni shell correlation emerges [46,47]. Comparable figures and insights for $Fe_{40}Ni_{40}B_{20}$ are provided in **sections S3-S5**; higher-shell signatures are less pronounced in that alloy.

From **Figs. 6** and **S5,** $Fe_{40}Ni_{40}P_{14}B_6$ shows an initial decrease in the first coordination-shell with increasing temperature, due to increased thermal vibrations, raising the DW factors (σ^2) accordingly. For Fe-P, σ^2 increases from $\sigma^2 = 2.55*10^{-2}(Å^2)$ (T = 300 K) over $\sigma^2 = 2.60*10^{-2}(Å^2)$ (T = 320 K) to $\sigma^2 = 2.81*10^{-2}(Å^2)$ (T = 420 K), then remains roughly constant until the phases changes significantly drop (Table 2), reflecting the development of greater local order. As crystallinity sets in, new peaks at higher R appear evidencing well-ordered next-nearest neighbour shells. For $Fe_{40}Ni_{40}B_{20}$ (Figs. S6-S9), the trend is similar across the heating programmes, except for a heating rate of 1.67 K/s, which shows a more gradual rise in χ(R). The steady amplitude increase with temperature suggests progressive structural relaxation that improves local ordering even before clear crystallisation; the more gradual rise at the fastest ramp may also reflect the limited growth time/temporal averaging at that rate.

3.3. *Structural model fitting of $Fe_{40}Ni_{40}P_{14}B_6$*

We now convert qualitative insights from the FT[χ(k)*k^3] of the k^3-weighted EXAFS into quantitative structural parameters [48]. A key outcome in this paper is the temperature- and rate-dependence of the DW factor - σ^2 - at the Fe- and Ni K-edges. Exemplary Figs. 7–8, and corresponding Tables 2–3 show the Fe- and Ni K-edge FT[χ(k)*k^3] spectra of $Fe_{40}Ni_{40}P_{14}B_6$ at a heating rate of 0.50 K/s. The spectra are well fitted using single-scattering paths derived from Fe_3P and Ni_3P crystal structures, consistent with the XRD-identified phases (**Section 3.1**).

Crystalline fits (cf. Fig. 7**(a)**) used single-scattering paths generated from crystallographic data Fe_3P [38] and Ni_3P [39] (tetragonal I-4 structure (space group 82)), representing contributions of five coordination shells - Fe-P, Fe-Fe_1, Fe-P_2, Fe-Fe_2 and Fe-Fe_3 - around the absorber. The amplitude reduction factor S_0^2 was fixed at 0.80 for Fe and 0.85 for Ni, which provided stable fits without unnecessary complexity. Notably, the phosphide-related peak (Fe/Ni–P scattering) is more pronounced in the Ni K-edge fits than in the Fe K-edge fits, indicating a stronger Ni–P coordination contribution. The remaining temperature-dependent EXAFS fits and tables as well as for the other heating ramps are provided in **section S4**.

Tables 4–5, summarise the refined bond distances R(Å) from the crystalline phases of Tables 2–3, and Tables S1-S8. The Fe-P distance refines slightly longer than the theoretical values, whereas Ni-P is only $\approx$ 0.01–0.07 Å above them. All metal-metal distances lie within the Fe_3P/Ni_3P ranges, which confirms that this alloy adopts the expected phosphide structure for all heating rates.

Coordination numbers are consistent with the expected local environments: for the Fe absorber, the first shell comprises 5 neighbours (2 metalloids + 3 metals (Fe-Fe_1)); for the Ni absorber, 10 neighbours (2 metalloids + 8 metals (Ni-Ni_1 + Ni-Ni_2)). Both the Fe and the Ni absorber see 4 P neighbours in its second coordination shell (Fe/Ni-P_2); subsequent shells include Fe-Fe_2 (3 Fe neighbours), Fe-Fe_3 (1 Fe neighbour), and Ni-Ni_3 (7 nickel neighbours).

During heating, σ^2 typically evolves in two stages: an initial rapid change (e.g. during heating) and a slower structural relaxation during

Table 2
Structural parameters from Fe K-edge EXAFS fitting of the sample $Fe_{40}Ni_{40}P_{14}B_6$ at a heating process of 0.50 K/s. S_0^2 as determined from Fe foil is fixed at 0.80 during the fits. k range for the FT for all fits was 1.996–11.858 $Å^{-1}$. Corresponds to Fig. 7 and Fig. S12.

	T = 1013 K, t = 34 min			**T = 1013 K, t = 10 min**			**T = 985 K**			**T = 695 K**			**T = 300 K**		
Path	$\Delta E_0 = 7.57(1.30)$ eV **R *factor*** = 0.00029			$\Delta E_0 = 3.21(1.53)$ eV **R *factor*** = 0.00223			$\Delta E_0 = 3.20(1.72)$ eV **R *factor*** = 0.00295			$\Delta E_0 = 3.78(1.51)$ eV **R *factor*** = 0.00278			$\Delta E_0 = -0.25(1.69)$ eV **R *factor*** = 0.00053		
	N	R(Å)	σ^2x10^2 ($Å^2$)	N	R(Å)	σ^2x10^2 ($Å^2$)	N	R(Å)	σ^2x10^2 ($Å^2$)	N	R(Å)	σ^2x10^2 ($Å^2$)	N	R(Å)	σ^2x10^2 ($Å^2$)
Fe-P	2	2.36 (0.01)	1.02 (0.20)	2	2.34 (0.01)	2.18 (0.33)	2	2.34 (0.01)	2.12 (0.35)	2	2.34 (0.01)	1.89 (0.31)	2	2.37 (0.02)	2.55 (0.46)
Fe-Fe1	3	2.46–2.62 (0.01)	0.53 (0.08)	3	2.44–2.60 (0.01)	1.12 (0.07)	3	2.44–2.59 (0.01)	1.13 (0.09)	3	2.44–2.59 (0.01)	1.10 (0.09)	3	2.43 – 2.58 (0.01)	0.67 (0.04)
Fe-P2	4	3.69–3.85 (0.03)	2.00 (0.55)	4	3.63–3.79 (0.04)	2.97 (0.69)	4	3.63–3.79 (0.05)	2.99 (0.79)	4	3.64 – 3.80 (0.04)	2.91 (0.77)	-	-	-
Fe-Fe2	3	4.37 – 4.41 (0.02)	0.90 (0.13)	3	4.32 – 4.35 (0.05)	2.33 (0.49)	3	4.33 – 4.36 (0.05)	2.37 (0.57)	3	4.33 – 4.36 (0.04)	2.00 (0.37)	-	-	-
Fe-Fe3	1	4.89 (0.02)	0.27 (0.17)	1	4.83 (0.07)	1.57 (0.92)	1	4.83 (0.07)	1.36 (0.77)	-	-	-	-	-	-

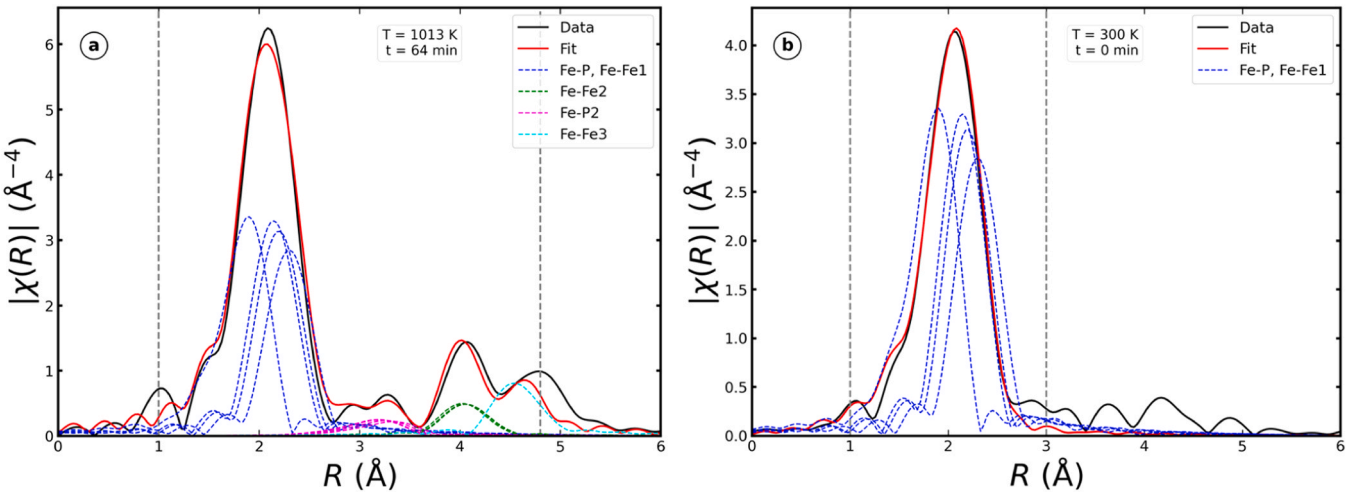

Fig. 7. Structural fits of the FT[χ(k)*k^3] of $Fe_{40}Ni_{40}P_{14}B_6$ at the Fe K-edge for two temperatures as indicated at a heating rate of 0.50 K/s. The fits match the data from the Fe K-edge for all phases, using the Fe_3P model (**Table 2** and **S3**). The dashed vertical lines indicate the fitting range of R_{min}= 1 Å to R_{max}= 4.8 Å (a) and R_{min}= 1 Å to R_{max}= 3 Å (b). Onset of crystallisation at T = (690 +/- 5) K. The rest of the evolution is provided in Fig. S12.

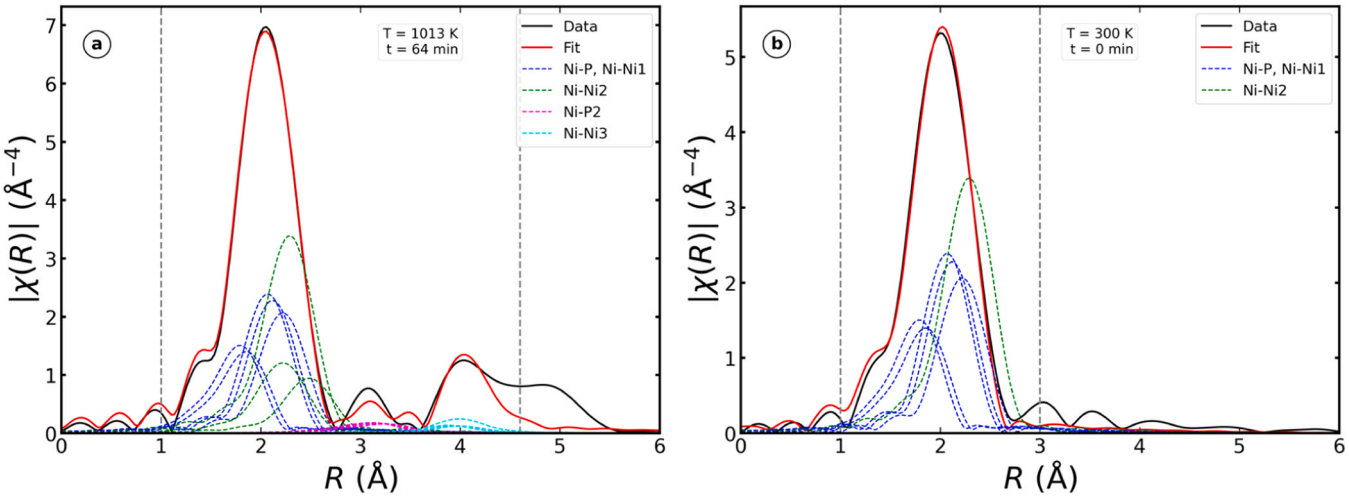

Fig. 8. Structural fits of the FT[χ(k)*k^3] of $Fe_{40}Ni_{40}P_{14}B_6$ at the Ni K-edge for different temperatures as indicated at a heating rate of 0.50 K/s. The fits match the data from the Ni K-edge for all phases, using the Ni_3P model (**Table 3** and **S4**). The dashed vertical lines indicate the fitting range of R_{min}= 1 Å to R_{max}= 4.6 Å (a) and R_{min}= 1 Å to R_{max}= 3 Å (b). Onset of crystallisation at T = (690 +/- 5) K. The rest of the evolution in figures is in Fig. S13.

isothermal hold. For the thermal component we tested Einstein and correlated Debye models [49]. The Einstein model (single effective frequency quantified by an Einstein temperature Θ_E) proved unstable for the Ni-P and Ni-Ni_1 shells over our wide temperature span, whereas the correlated Debye model (continuous spectrum of phonon frequencies up to a Debye temperature Θ_D) provided consistent fits across the entire ramp. We therefore use the Debye model for σ^2(T) during heating. For the isothermal segment, a Johnson–Mehl–Avrami-Kolmogorow (JMAK) description [50,51] tended to overfit in some cases during analysis [52]; we therefore adopt a stretched-exponential (Kohlrausch–Williams–-Watts) [53] form, which robustly captures the observed relaxation kinetics.

To evaluate and compare the evolution of the DW factors for Fe–P vs Ni–P and Fe–Fe_1 vs Ni–Ni_1, we also fitted a simple logarithmic model to σ^2 (with $\pm1\sigma_s$ statistical uncertainty confidence intervals as semi-transparent envelopes), aiming to confirm general trends.

Metal-metal shells (Table 6) consistently yield a small σ^2 in the crystalline state, indicating a well-ordered Fe/Ni sublattice. Metal-metalloid shells show a slightly larger disorder, consistent with the stronger vibration of the lighter P atoms. On average, Ni-P σ^2 are around 15 % lower than Fe-P σ^2, because Ni_3P generally exhibits a higher enthalpy of formation compared to Fe_3P (-45 kJ/mol for Fe_3P [54] vs −200 kJ/mol for Ni_3P [55]), indicating that Ni_3P is thermodynamically more stable.

Additionally, **Tables 2-3**, **S1-S8**, Figs. 9–10 show, that in the amorphous state, σ^2 increases with temperature (thermal disorder), producing broader, lower χ(R) peaks. At the onset of crystallisation, σ^2 drops sharply as ordered phases form. Both phenomena are more notable for Fe than for Ni, indicating that Fe-centred order develops earlier. After full crystallisation and post-annealing, σ^2 stabilises at a lower level; the system reaches a stable, ordered state with minimal further (or none) reduction in disorder, consistent with literature trends [6].

The comparative σ^2(t) evolution for Fe/Ni-P and Fe/Ni-Fe_1/Ni_1 is shown in **Fig. 11** and **S18**. All series follow a logarithmic trend; the fitted slope *b* of each coordination shell quantifies the rate and direction of its change in disorder. For Fe/Ni-P, b< 0 ((●), respectively (●)) at all heating rates, indicating decreasing disorder and strengthening energetically favourable metal-metalloid bonding during early crystallisation stages. For Fe-Fe and Ni-Ni, b> 0 ((●), respectively (●)) at all rates except the fastest at 1.67 K/s, consistent with the delayed build-up or partial

Table 3
Structural parameters from Ni K-edge EXAFS fitting of the sample $Fe_{40}Ni_{40}P_{14}B_6$ at a heating process of 0.50 K/s. S_0^2 as determined from Fe foil is fixed at 0.85 during the fits. k range for the FT for all fits was 2.072–10.752 $Å^{-1}$. Corresponds to Fig. 8 and Fig. S13.

	T = 1013 K, t = 34 min			T = 1013 K, t = 10 min			T = 985 K			T = 695 K			T = 300 K		
Path	ΔE_0 = 9.29(1.66) eV **R *factor*** = 0.00014			ΔE_0 = 6.10(1.56) eV **R *factor*** = 0.00032			ΔE_0 = 5.87(1.57) eV **R *factor*** = 0.00064			ΔE_0 = 6.29(1.91) eV **R *factor*** = 0.00010			ΔE_0 = -4.43(5.50) eV **R *factor*** = 0.00011		
	N	R(Å)	σ^2x10^2 ($Å^2$)	N	R(Å)	σ^2x10^2 ($Å^2$)	N	R(Å)	σ^2x10^2 ($Å^2$)	N	R(Å)	σ^2x10^2 ($Å^2$)	N	R(Å)	σ^2x10^2 ($Å^2$)
Ni-P	2	2.29–2.36	1.29	2	2.29–2.35	2.41	2	2.29–2.35	2.44	2	2.29–2.35	2.43	2	2.22–2.29	3.70
		(0.02)	(0.36)		(0.02)	(0.38)		(0.02)	(0.39)		(0.02)	(0.46)		(0.04)	(1.07)
Ni-Ni1	3	2.45–2.60	0.46	3	2.41–2.56	0.95	3	2.41–2.56	0.98	3	2.42–2.57	0.87	3	2.38–2.53	0.75
		(0.01)	(0.13)		(0.01)	(0.13)		(0.01)	(0.14)		(0.01)	(0.13)		(0.01)	(0.11)
Ni-Ni2	5	2.61–2.87	1.80	5	2.59–2.85	1.95	5	2.58–2.84	1.97	5	2.59–2.85	1.91	3	2.46	2.36
		(0.03)	(0.52)		(0.02)	(0.33)		(0.02)	(0.35)		(0.02)	(0.35)		(0.14)	(0.57)
Ni-P2	4	3.74–3.90 (0.05)	2.31	4	3.70–3.86 (0.04)	2.89	4	3.70–3.86 (0.04)	2.91	4	3.70–3.86 (0.05)	2.90	-	-	-
			(0.69)			(0.60)			(0.61)			(0.72)			
Ni3	7	4.32–4.44 (0.02)	1.43 (0.18)	7	4.27–4.40 (0.03)	2.59 (0.35)	7	4.27–4.40 (0.04)	2.63 (0.36)	7	4.27–4.39 (0.04)	2.73 (0.47)	-	-	-

coarsening of metal-metal correlations. The narrow confidence bands confirm that the logarithmic law captures σ^2 trends robustly.

Overall, these observations highlight the interplay between local ordering (preferential metal-metalloid bonding) and long-range reorganisation (growth of metal-metal networks), and underscore why combining QEXAFS with XRD is essential for a complete interpretation of the annealing process.

3.4. Structural model fitting of $Fe_{40}Ni_{40}B_{20}$

QEXAFS data for $Fe_{40}Ni_{40}B_{20}$ were fitted with single-scattering paths generated from orthorhombic Fe_3Ni_3B (Pnma, space group 62) [40,41], identified by in-situ XRD (**Section 3.1**). For the crystalline state, we used Fe_3B (Fe) and Ni_3B (Ni) prototypes as starting geometries, consistent with the results obtained from XRD. All fits were performed on k ^{3} -weighted χ(k) data using Artemis [37], (Tables S9-S12).

Best-fit distances (R(Å)) agree well with Fe_3B structural parameters: Fe-B refines to R= 2.08–2.18 + /- 0.04 Å (theory: R=2.02–2.12 Å) and Fe-Fe_1 refines to R= 2.38–2.58 + /- 0.01 Å (theory: R=2.41–2.60 Å). At the Ni edge, Ni-B and Ni-Ni_1 converge to R= 1.97 + /- 0.02 Å (theory: R = 1.98 Å), and R= 2.37–2.54 + /- 0.01 Å (theory: R=2.40–2.57 Å); in both cases for a heating rate of 1.67 K/s. The 0.25 K/s analysis (Tables S9-S10) shows a similar behaviour. Together, these results support orthorhombic $(Fe,Ni)_3B$ as the dominant crystalline phase, in agreement with XRD. The refined coordination environment is consistent with the boride prototypes: the Fe absorber has 7 neighbours (2 metalloids + 5 metals (Fe-Fe_1)), as well as the Ni absorber (1 metalloid + 6 metals (Ni-Ni_1)). Refined DW factors (σ^2x10^2 ($Å^2$)) for the fully crystalline phase for two heating rates are listed in Table 7.

The metal-metal shells (Table 7) are almost identical at both rates, indicating a similar order once crystallisation is complete. The metal-metalloid shells show larger σ^2 and higher uncertainties, reflecting the weaker scattering of Boron. The slower ramp exhibits a higher σ^2, consistent with longer exposure in the transformation window and support of a minor Boron redistribution. Across heating programmes, σ^2 for metal-metalloid shells drops substantially between the amorphous and crystalline states, confirming that thermal and static disorder are largely removed upon crystallisation.

3.5. Wavelet transform and concluding results

As an independent check on the EXAFS-derived transitions, wavelet transforms (Morlet; MorletE software [56] **Figs. 14** and **S23** for $Fe_{40}Ni_{40}P_{14}B_6$, and Figs. S24-S25 for $Fe_{40}Ni_{40}B_{20}$) of the χ(k) data are computed. Alloy data are compared with reference foils (Fe, Ni; measured at P64) and with simulated Fe_3P and Ni_3P data ($Fe_{40}Ni_{40}P_{14}B_6$), respectively Fe_3B and Ni_3B data ($Fe_{40}Ni_{40}B_{20}$) derived from their crystallographic structures. The reference foils show a sharp, high-intensity section near R≈ 2.1 Å, k ≈ 8 $Å^{-1}$ for both, the Fe and Ni foil, plus weaker contributions for R > 3 Å.

In the amorphous state, both alloys exhibit a single broad section, consistent with a complete absence of medium-range order. Upon heating, the main section of $Fe_{40}Ni_{40}P_{14}B_6$ shows sharpening and subtle secondary features appear, signalling the onset of further order. These match the Fe_3P/Ni_3P simulations, confirming phosphide -like crystallisation. For $Fe_{40}Ni_{40}B_{20}$, amorphous-to-crystalline differences are more subtle, reflecting the limited *k*- and R-range used in first shell fits. We see however, intensity gain and a slight shift to higher *k* around R≈ 2.1 Å, at both edges, and a modest sharpening of the first-shell Fe-Fe/Ni-Ni correlation - evolving from a broad rounded profile towards a form that resembles the main section of the pristine Fe/Ni foil.

During annealing, $Fe_{40}Ni_{40}P_{14}B_6$ rapidly develops second- and third-shell EXAFS features, indicating robust build-up of medium-range order, consistent with a Ni_3P contribution. In $Fe_{40}Ni_{40}B_{20}$, higher-R features emerge more slowly and remain weaker, suggesting either a slower evolution of medium-range order or finer nanocrystalline

Table 4
Summary of the Fe refined bond distances R(Å) for two metalloid (M - P) and three metal (M - M) shells for all 4 heating rates of $Fe_{40}Ni_{40}P_{14}B_6$. Errors are given in parentheses.

Heating rate	Fe-P	Fe-Fe_1	Fe-P_2	Fe-Fe_2	Fe-Fe_3
0.25 K/s	2.31 (0.01)	2.47–2.62 (0.01)	3.68–3.84 (0.03)	4.35–4.39 (0.02)	4.87 (0.03)
0.50 K/s	2.36 (0.01)	2.46–2.62 (0.01)	3.69–3.85 (0.03)	4.37–4.41 (0.02)	4.89 (0.02)
0.67 K/s	2.32 (0.01)	2.47–2.63 (0.01)	3.69–3.85 (0.03)	4.37–4.41 (0.02)	4.88 (0.02)
1.67 K/s	2.36 (0.01)	2.45–2.61 (0.01)	3.66–3.82 (0.03)	4.34–4.38 (0.02)	4.86 (0.02)
R(Å) (theory):	2.26	2.47–2.63	3.76–3.92	4.31–4.34	4.73

Table 5
Summary of the Ni refined bond distances R(Å) for two metalloid (M - P) and three metal (M - M) shells for all 4 heating rates of $Fe_{40}Ni_{40}P_{14}B_6$. Errors are given in parentheses.

Heating rate	Ni-P	Ni-Ni_1	Ni-P_2	Ni-Ni_2	Ni-Ni_3
0.25 K/s	2.23–2.30 (0.02)	2.45–2.60 (0.02)	2.57–2.84 (0.04)	3.70–3.86 (0.05)	4.29–4.42 (0.03)
0.50 K/s	2.29–2.36 (0.02)	2.45–2.60 (0.01)	2.61–2.87 (0.03)	3.74–3.90 (0.05)	4.32–4.44 (0.02)
0.67 K/s	2.23–2.30 (0.02)	2.47–2.61 (0.02)	2.54–2.81 (0.06)	3.70–3.86 (0.05)	4.29–4.42 (0.02)
1.67 K/s	2.29–2.36 (0.02)	2.46–2.61 (0.01)	2.61–2.87 (0.04)	3.76–3.91 (0.07)	4.32–4.45 (0.03)
R(Å) (theory):	2.22–2.29	2.44–2.58	2.65–2.91	3.70–3.86	4.26–4.39

Table 6
Summary of the refined σ^2 values (σ^2x10^2 ($Å^2$)) for the first metalloid (M - P) and first metal (M - M) shells for all 4 heating rates of $Fe_{40}Ni_{40}P_{14}B_6$.

Heating rate	Fe-P	Fe-Fe_1	Ni-P	Ni-Ni_1
0.25 K/s	1.29 + /- 0.19	0.76 + /- 0.08	0.99 + /- 0.26	0.68 + /- 0.11
0.50 K/s	1.02 + /- 0.20	0.53 + /- 0.08	1.29 + /- 0.36	0.46 + /- 0.13
0.67 K/s	1.01 + /- 0.15	0.57 + /- 0.07	0.67 + /- 0.23	0.52 + /- 0.12
1.67 K/s	1.28 + /- 0.27	0.50 + /- 0.07	1.08 + /- 0.34	0.62 + /- 0.14

domains. Essentially, the Phosphorous-containing glass shows a more pronounced long-range structural order upon crystallisation than the Boron glass, which implies differences in their crystallisation behaviour: Phosphorous promotes the formation of intermetallic compounds - strong multi-shell EXAFS signals, whereas Boron-only compositions initially crystallise in a more constrained or finer way, which yields less pronounced EXAFS features from distant shells.

Additional XAS measurements were acquired at the DELTA storage ring (Dortmund, Germany) [57,58] (**section S9**): the magnitude of the Fourier transform FT[χ(k)*k^3] of the k^3-weighted EXAFS displays the Fe-P shell with higher amplitude for the 77 K amorphous spectrum, whereas the 300 K spectrum is broader and more damped, which is consistent with a well-known increase in the DW factor at elevated temperatures [59]. Upon crystallisation, χ(R) resolves into multiple peaks, evidencing the build-up of ordered coordination shells. The cryogenic spectrum remains amorphous; additional higher-order peaks observed during heating reflect structural ordering rather than thermal effects. Cryogenic data of the post-annealed state are not discussed further; apart from the expected amplitude gain, peak positions and overall motif are unchanged, adding no new information.

Finally, EXAFS and XRD provide a consistent, time-resolved picture: XRD records the first Bragg reflections at the onset of crystallisation, while EXAFS shows a rise in |χ(R)| and a drop in the DW factors - σ^2. Once Bragg peaks appear in XRD, EXAFS amplitudes increase, confirming local ordering; XRD-based phase identification secures the scattering paths used in the EXAFS fits. After the isothermal annealing,

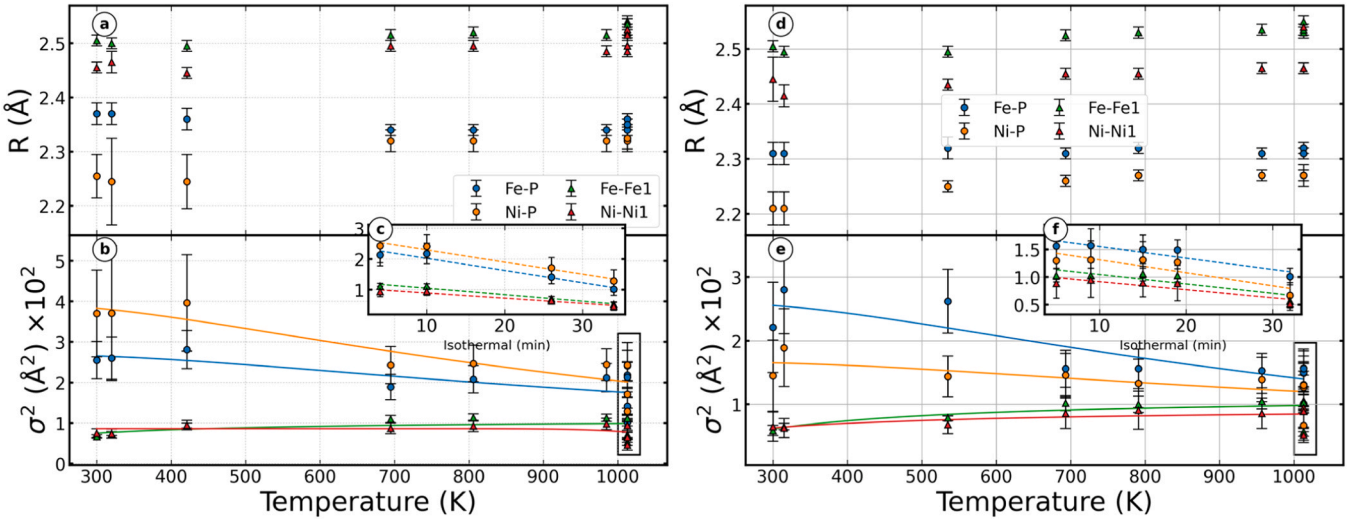

Fig. 9. (a)/(d) show the bond distance R vs temperature for Fe–P/Ni–P and Fe–Fe1/Ni–Ni1 shells obtained from Fe/Ni K-edge EXAFS fitting of $Fe_{40}Ni_{40}P_{14}B_6$ at a heating process of 0.50 K/s (left) and 0.67 K/s (right). (b)/(e) display the squared Debye-Waller factors vs temperature with overlaid Debye model fits (solid lines). The insets (c)/(f) present the isothermal annealing and structural relaxation at T = (1013 +/- 50) K fitted by a stretched-exponential function (dashed lines). All fits withstand the routine check.

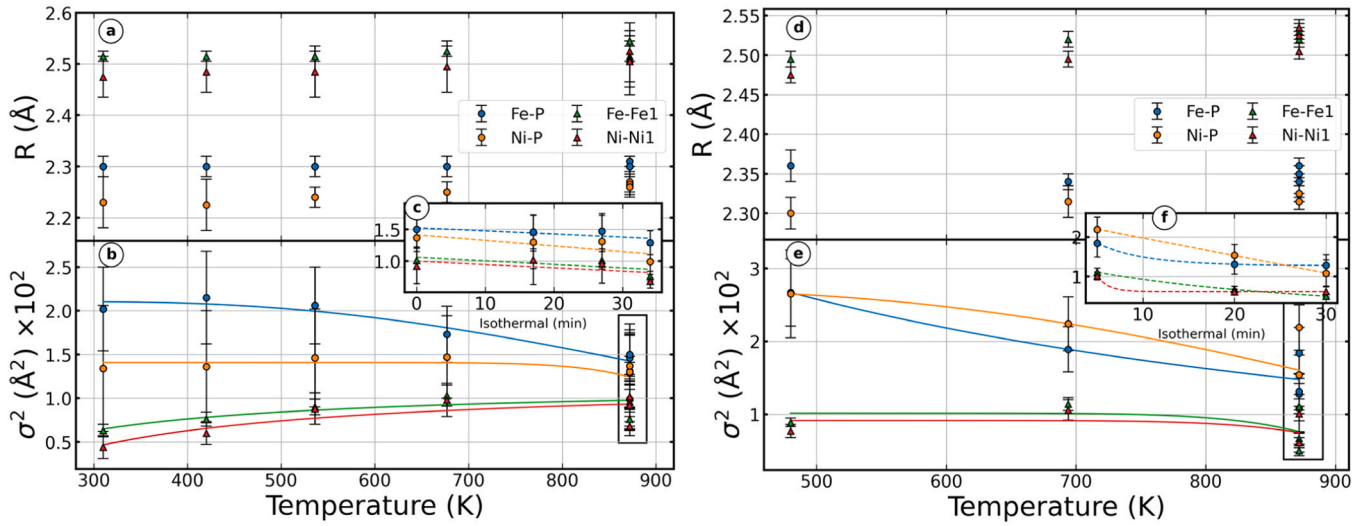

Fig. 10. (a)/(d) show the bond distance R vs temperature for Fe–P/Ni–P and Fe–Fe1/Ni–Ni1 shells obtained from Fe/Ni K-edge EXAFS fitting of $Fe_{40}Ni_{40}P_{14}B_6$ at a heating process of 0.25 K/s (left) and 1.67 K/s (right). (b)/(e) display the squared Debye-Waller factors vs temperature with overlaid Debye model fits (solid lines). The insets (c)/(f) present the isothermal annealing and structural relaxation at T = (872 +/- 50) K fitted by a stretched-exponential function (dashed lines). All fits withstand the routine check.

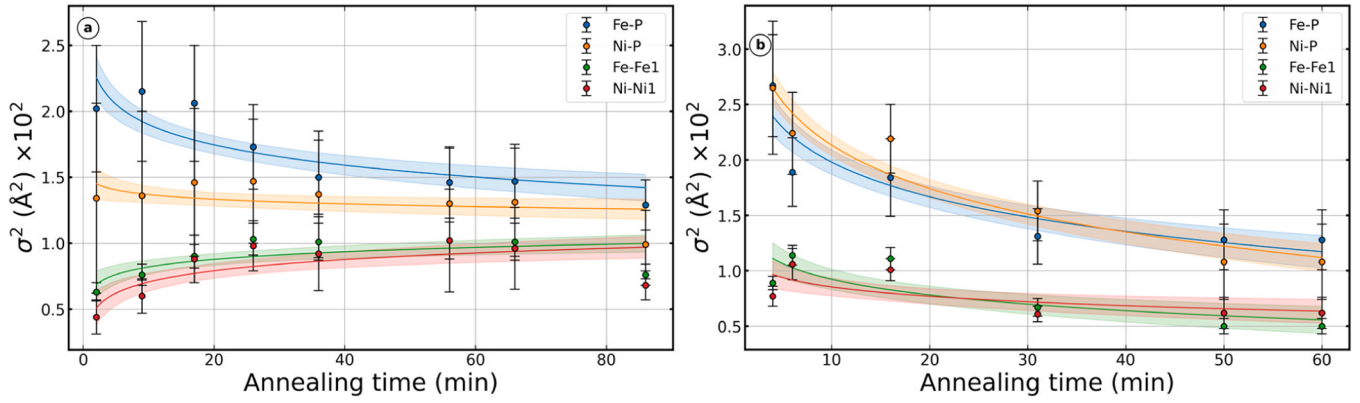

Fig. 11. DW factor evolution comparison of $Fe_{40}Ni_{40}P_{14}B_6$ over time (annealing + isothermal annealing) at a heating process of 0.25 K/s (a) and 1.67 K/s (b). The displayed curves describe a logarithmic behaviour with $\pm 1\sigma_s$-bands (statistical uncertainty) and changes: (a): b = -0.22 *ln(t) (●), b = -0.05 * ln(t) (●), b = +0.08 * ln (t) (●) and b = +0.12 * ln(t) (●), (b): b = -0.45 *ln(t) (●), b = -0.57 * ln(t) (●), b = -0.21 * ln(t) (●) and b = -0.12 * ln(t) (●).

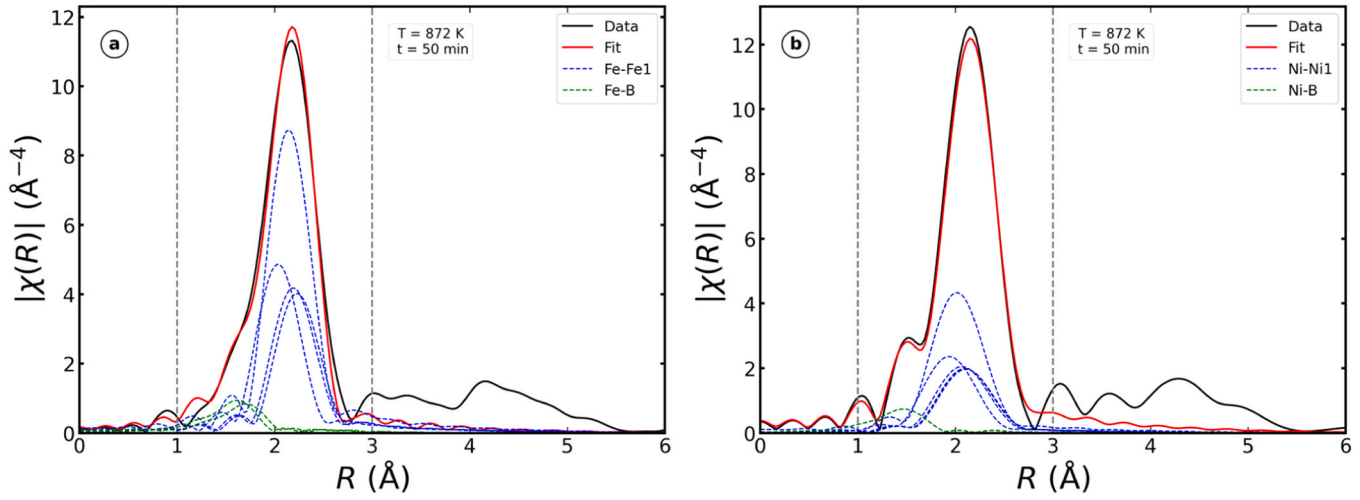

Fig. 12. Structural fits of the FT[χ(k)*k³] of $Fe_{40}Ni_{40}B_{20}$ at a heating rate of 1.67 K/s for Fe - left and Ni - right. The fits match the data from the Fe/Ni K-edge for all phases, using the Fe_3B/Ni_3B model (Tables S11 and S12). The dashed vertical lines indicate the fitting range of R= 1 Å to 3 Å for all graphs**.** Onset of crystallisation at T = (825 +/- 50) K. Full set for both Fe and Ni provided in **section S5**.

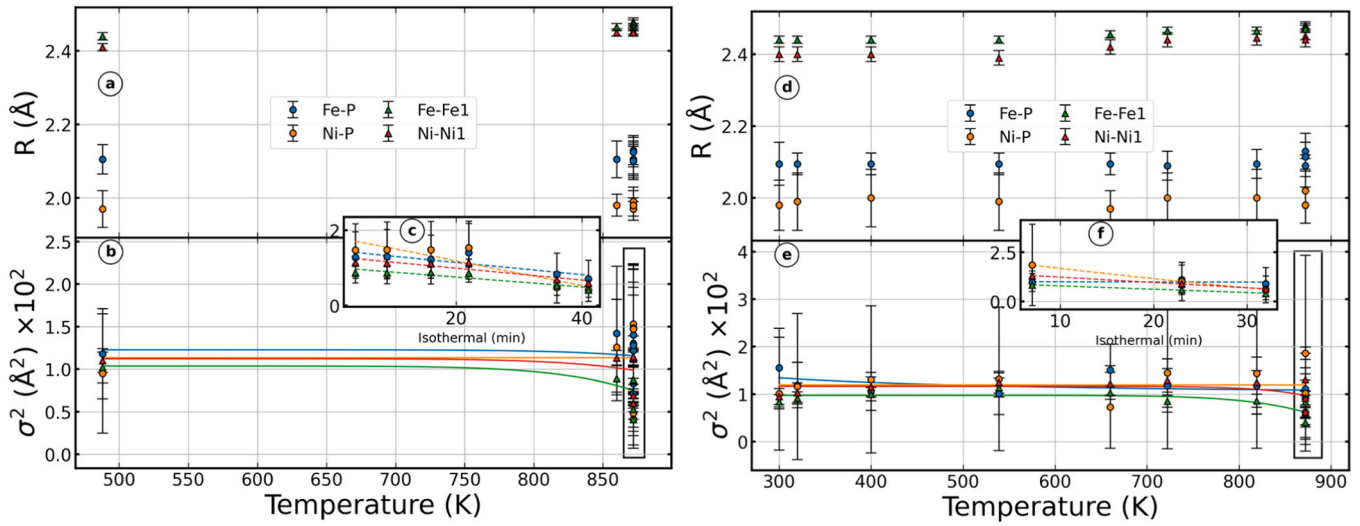

Fig. 13. (a)/(d) show the bond distance R vs temperature for Fe–B/Ni–B and Fe–Fe1/Ni–Ni1 shells obtained from Fe/Ni K-edge EXAFS fitting of $Fe_{40}Ni_{40}B_{20}$ at a heating process of 1.67 K/s (left) and 0.25 K/s (right). (b)/(e) display the squared DW factors vs temperature with overlaid Debye model fits (solid lines). The insets (c)/(f) present the isothermal annealing and structural relaxation at T = (872 +/- 50) K fitted by a stretched-exponential function (dashed lines). All fits withstand the routine check.

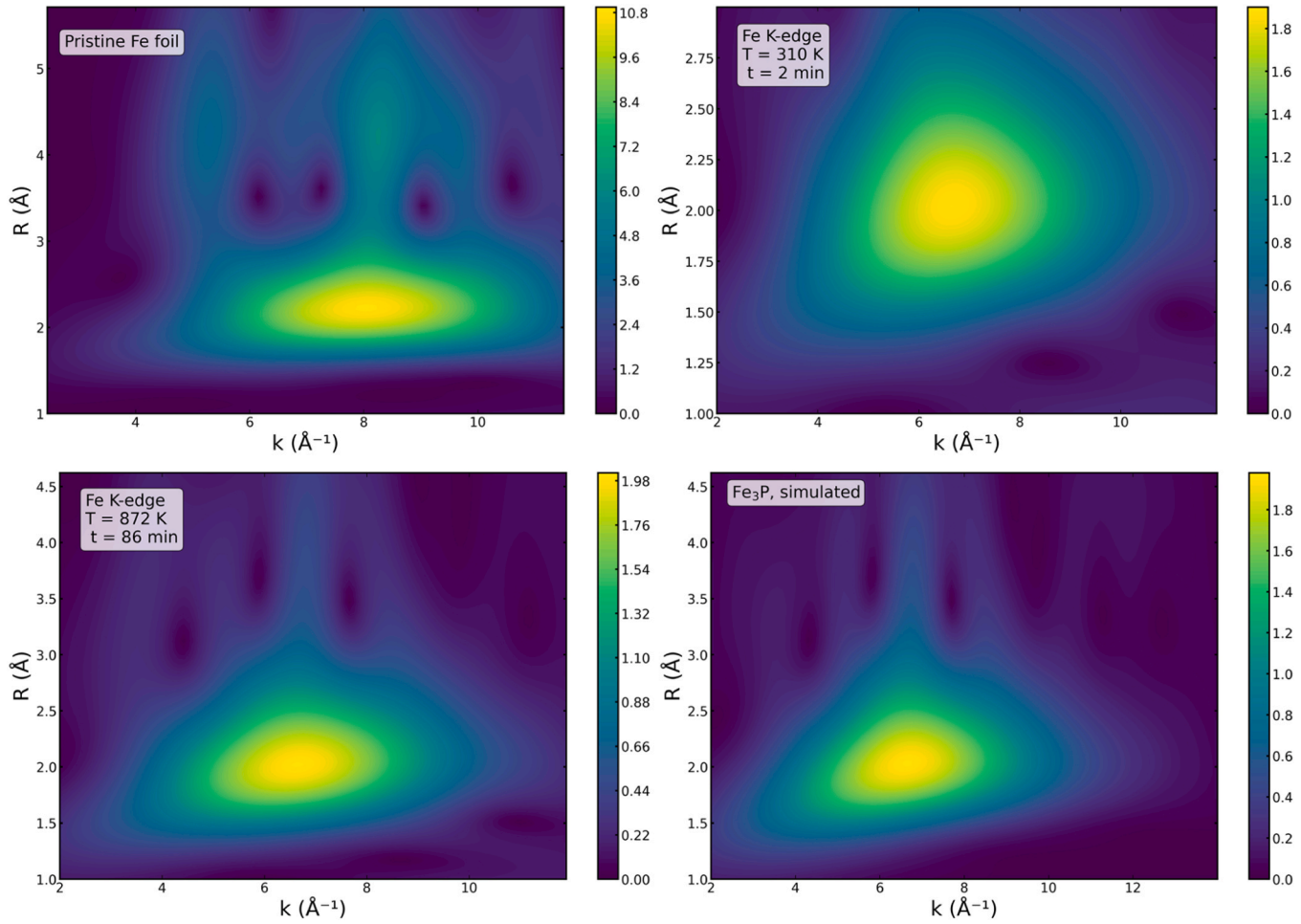

Fig. 14. Two-dimensional contour maps of the Fe K-edge Morlet wavelet transform. In comparison are pristine Fe foil (top left), $Fe_{40}Ni_{40}P_{14}B_6$ in the amorphous state (top right), $Fe_{40}Ni_{40}P_{14}B_6$ in the crystalline state (bottom left) and the simulated Fe_3P reference derived from its crystallographic structure. The colour scale denotes each of the wavelet amplitudes, with brighter regions indicating stronger contributions from the k and R ranges.

Table 7
Summary of the refined σ^2 values ($\sigma^2 x10^2$ (Å^2)) for the first metalloid (M - P) and first metal (M - M) shells for both heating rates of $Fe_{40}Ni_{40}B_{20}$.

Heating rate	Fe-B	Fe-Fe_1	Ni-B	Ni-Ni_1
0.25 K/s	0.91 + /- 0.82	0.41 + /- 0.10	0.62 + /- 0.68	0.63 + /- 0.11
1.67 K/s	0.71 + /- 0.49	0.41 + /- 0.09	0.41 + /- 0.30	0.60 + /- 0.06

both techniques stabilise: σ^2 reaches a minimum and the main Bragg peaks narrow.

4. Conclusion

We have shown a detailed view of the crystallisation process in $Fe_{40}Ni_{40}P_{14}B_6$ and $Fe_{40}Ni_{40}B_{20}$ metallic glasses through a combined simultaneous approach of in-situ time-resolved XRD and multi-edge (Fe + Ni) quick-scanning EXAFS analysis. Both alloys follow an anticipated phase transformation during annealing and isothermal annealing: $Fe_{40}Ni_{40}P_{14}B_6$ crystallises for all observed heating ramps into tetragonal Ni_3P and γ-Fe (face-centred cubic), while $Fe_{40}Ni_{40}B_{20}$ crystallises into orthorhombic $(Fe,Ni)_3B$ and γ-(Fe,Ni) (face-centred cubic). The onset of crystallisation for $Fe_{40}Ni_{40}P_{14}B_6$ is in line with literature and the onset of crystallisation for $Fe_{40}Ni_{40}B_{20}$ lies close to reported values. Onsets and subsequent evolution were marked by the appearance of characteristic Bragg peaks in XRD, a simultaneous inversion of spectral features in XANES and analysis of EXAFS features. Element-specific observations showed that new Fe–Fe and Ni–Ni coordination shells appear and intensify in the EXAFS signals, as crystallisation proceeds, which tracks the growth of structural ordering of the nearest-neighbours. EXAFS fitting further confirmed that DW factors decrease during heating and isothermal hold, indicating a reduction in local disorder.

The difference in crystallisation dynamics between $Fe_{40}Ni_{40}P_{14}B_6$ which develops medium-to long-range order rather quickly, whereas $Fe_{40}Ni_{40}B_{20}$ shows a more gradual, subtle evolution of its higher-shell EXAFS features, suggesting a slower growth or finer nanocrystalline domains in the boron-containing glass. Notably, in this multi-edge QEXAFS approach, Fe-centred shells relax and crystallise sooner than Ni-centred shells; Ni-P/B bonds remain tighter, while Fe-Fe disorder transiently increases as Fe rich clusters form. These trends could only be resolved with this element-specific dual-edge approach. Heating-rate effects are consistent with kinetics: slower ramps allow more pre-ordering, while faster ramps (e.g. 1.67 K/s) require a longer isothermal period to reach a similar low-σ^2 plateau. Cross-validation of Fe-and Ni-specific disorder with analysed Bragg peaks via XRD, provides a consistent, element-resolved picture of the transformation from amorphous to crystalline. Cryogenic baseline experiments (amorphous data at T = 77 K) confirmed that additional EXAFS peaks at elevated temperature arise from structural ordering, not merely thermal vibrations.

We also introduced a lightweight Python script that parses Artemis fit files, matches path-specific ΔR and σ^2 errors (with planned extensions), and produces rounded, one-line summaries - useful for routine EXAFS reporting and reproducibility. In our in-situ protocol the crystallisation of the 7–15 μm foils was irreversible, and the foils embrittle on cooldown/removal from the heating dome; consequently, specimens were not recoverable for TEM thinning after the runs. As a follow-up, ex-situ TEM on ribbons annealed under replicated thermal histories (matching set-point rates and holds) could be performed. This would directly assess grain size distributions, and phase identity/fractions, providing an independent validation of the kinetics inferred from QEXAFS-XRD.

The approach in this work can be used to deconstruct complex phenomena, such as optimising annealing treatments for magnetic performance in Fe-based ribbons or understanding multi-component rearrangements in biomaterials and bioactive glasses - thereby improving reliability in medical implants. Amorphous alloys are often considered for radiation shielding (e.g. neutron-absorbing borated glasses) and for components in nuclear/space applications that must endure thermal extremes; our methodology offers a way to test how such materials respond under quick heating or prolonged irradiation. Insights could open possibilities for the development of shielding materials that keep their amorphous structure under stress or intentionally crystallise into phases that enhance shielding effectiveness.

Finally, we are planning to upload selected Fe/Ni K-edge XAS spectra for the samples and references to the *RefXAS* (http://xafsdb.ddns.net/) database under an open access policy [60–62].

Funding sources

This publication was written in the context of the work of the consortium DAPHNE4NFDI in association with the German National Research Data Infrastructure (NFDI). NFDI is financed by the Federal Republic of Germany and the 16 federal states, and the consortium is funded by the Deutsche Forschungsgemeinschaft (project No. 460248799). The authors would like to thank for the funding and support. Furthermore, thanks go to all institutions and actors who are committed to the association and its goals. The authors would like to thank CRC1441 for further financial support (project No. 426888090).

CRediT authorship contribution statement

Dirk Lützenkirchen-Hecht: Writing – review & editing, Supervision, Project administration, Funding acquisition. **Abhijeet Gaur:** Writing – review & editing, Validation, Investigation, Formal analysis. **Sebastian Paripsa:** Writing – review & editing, Writing – original draft, Visualization, Software, Methodology, Investigation, Formal analysis, Conceptualization.

Declaration of Competing Interest

The authors declare that they have no known competing financial interests or personal relationships that could have appeared to influence the work reported in this paper.

Acknowledgements

We acknowledge DESY (Hamburg, Germany), a member of the Helmholtz Association HGF, and DELTA (Dortmund, Germany), for the provision of experimental facilities. Parts of this research were carried out at PETRA III (DESY). Data was collected using beamlines P64 operated/provided by DESY Photon Science, and beamline 10 operated/provided by DELTA synchrotron facility. We would like to thank W. Caliebe, E. Welter and L. Voss for assistance during the experiments. Special thanks to F. Förste for reviewing the manuscript.

Appendix A. Supporting information

Supplementary data associated with this article can be found in the online version at doi:10.1016/j.jallcom.2025.184136.

References

[1] W. Klement, R. Willens, P. Duwez, Non-crystalline structure in solidified Gold–Silicon alloys, Nature 187 (1960) 869–870, https://doi.org/10.1038/187869b0.
[2] M.M. Khan, A. Nemati, Z.U. Rahman, U.H. Shah, H. Asgar, W. Haider, Recent advancements in bulk metallic glasses and their applications: a review, Crit. Rev. Solid State Mater. Sci. 43 (3) (2017) 233–268, https://doi.org/10.1080/10408436.2017.1358149.

[3] R.Z. Noorbakhsh, F. Ostovan, M. Toozandehjani, Fe-Based amorphous alloy coatings: a review, Adv. Eng. Mater. 26 (2024) 2302184, https://doi.org/10.1002/adem.202302184.

[4] S. Lu, M. Wang, Z. Zao, Recent advances and future developments in Fe-based amorphous soft magnetic composites, J. Non Cryst. Solids 646 (2023) 122440, https://doi.org/10.1016/j.jnoncrysol.2023.122440.

[5] A. Inoue, F. Kong, X. Zhu, J. Chen, H. Men, W.J. Botta, Development and industrialization of Zr- and Fe-based bulk metallic glasses and light metal-based metastable alloys, J. Alloy. Compd. 979 (2024) 173546, https://doi.org/10.1016/j.jallcom.2024.173546.

[6] N. Hayen, P. Jordt, S.C. Hövelmann, L. Petersdorf, M. Mewes, L. Thormählen, D. Meyners, N.X. Sun, C. Sternemann, M. Paulus, D. Lützenkirchen-Hecht, B. M. Murphy, In situ X-Ray absorption studies on local structure of annealed metallic glasses FeGaB and FeCoSiB, Phys. Status Solidi A (2024) 2400607, https://doi.org/10.1002/pssa.202400607.

[7] N. Chakri, B. Bendjemil, M. Baricco, Crystallization kinetics and magnetic properties of $Fe_{40}Ni_{40}B_{20}$ bulk metallic glass, Adv. Chem. Eng. Sci. 4 (2014) 36–38, https://doi.org/10.4236/aces.2014.41005.

[8] E.A. Sviridova, S.V. Vasiliev, V.I. Tkatch, Analysis of suppression conditions of $Fe_{40}Ni_{40}P_{14}B_6$ melt crystallization, Phys. Met. Met. 124 (2023) 885–893, https://doi.org/10.1134/S0031918X23601440.

[9] H. Brodowsky, H. Sagunski, Diffusion of boron in the metallic glass $Fe_{40}Ni_{40}B_{20}$, Z. Phys. Chem. Neue Folge 139 (1984) 149–152, https://doi.org/10.1524/zpch.1984.139.139.149.

[10] M. Takahashi, M. Koshimura, T. Abuzuka, Phase diagram of amorphous and crystallized Fe-B alloy system, Jpn. J. Appl. Phys. 20 (1981) 1821, https://doi.org/10.1143/JJAP.20.1821.

[11] B. Yang, J.W.P. Schmelzer, B. Zhao, Y. Gao, C. Schick, Glass transition and primary crystallization of $Al_{86}Ni_6Y_{4.5}Co_2La_{1.5}$ metallic glass at heating rates spanning over six orders of magnitude, Scr. Mater. 162 (2019) 146–150, https://doi.org/10.1016/j.scriptamat.2018.11.014.

[12] Y. Wang, Z. Hao, Y. Zhang, X. Liang, X. Bai, C. Cao, Formation of $L1_0$-FeNi hard magnetic material from FeNi-based amorphous alloys, Chin. Phys. B. 31 (2022) 046301, https://doi.org/10.1088/1674-1056/ac280a.

[13] S.V. Vasiliev, O.V. Kovalenko, K.A. Svyrydova, A.I. Limanovskii, V.I. Tkatch, Crystallization kinetics of the $Fe_{40}Ni_{40}P_{14}B_6$ metallic glass in an extended range of heating rates, J. Mater. Sci. 54 (2019) 5788–5801, https://doi.org/10.1007/s10853-018-03225-6.

[14] B. Gu, F. Liu, Y.Z. Chen, Y.H. Jiang, Y.Z. Ma, Structural modification and phase transformation kinetics: crystallization of amorphous $Fe_{40}Ni_{40}P_{14}B_6$ eutectic alloy, J. Mater. Sci. 49 (2014) 842–857, https://doi.org/10.1007/s10853-013-7768-9.

[15] B. Bendjemil, N.E. Chakri, J. Bougdira, E. Ferrara, F. Vinai, M. Baricco, Crystallization kinetics and magnetic properties of $Fe_{40}Ni_{40}B_{20}$ amorphous ribban, J. Chem. Eng. Mater. Sci. 3 (2014) 93–95, https://doi.org/10.13189/cme.2014.020401.

[16] T. Watanabe, M. Scott, The crystallization of the amorphous alloy $Fe_{40}Ni_{40}P_{14}B_6$, J. Mater. Sci. 15 (1980) 1131–1139, https://doi.org/10.1007/BF00551801.

[17] N.K. Gobran, M.M. Danial, R. Kamel, Kinetics of the amorphous-crystalline transition in the metallic glass $Fe_{40}Ni_{40}B_{20}$, Phys. Status Solidi A 82 (1984) 63–66, https://doi.org/10.1002/pssa.2210820107.

[18] M. Stubičar, E. Babić, D. Subašić, D. Pavuna, Ž. Marohnić, Phase transformations during isochronal annealing of $Fe_{40}Ni_{40}B_{20}$ glass, 334, Phys. Status Solidi A 44 (1977) 339, https://doi.org/10.1002/pssa.2210440136.

[19] J. Čermák, M. Čerňanský, P. Duhaj, J. Horváth, Crystallization of the metallic glass $Fe_{40}Ni_{40}B_{20}$ during isochronal annealing in argon and hydrogen, Phys. Status Solidi A 91 (1985) 407–410, https://doi.org/10.1002/pssa.2210910208.

[20] M.G. Scott, The crystallization kinetics of Fe-Ni based metallic glasses, J. Mater. Sci. 13 (1978) 291–296, https://doi.org/10.1007/BF00647772.

[21] P. Huang, Y. Shi, W. Zhang, S. Zhang, Y. Ren, K. Qiu, J. Wang, Phase evolution and glass formation in an Fe-Based alloy, Acta Metall. Sin. (Engl. Lett. 36 (2023) 1502–1510, https://doi.org/10.1007/s40195-023-01565-0.

[22] D. Koningsberger, R. Prins, X-ray absorption. Principles. Applications and Techniques of EXAFS, SEXAFS, and XANES, John Wiley & Sons, New York, 1988.

[23] E. Zolotoyabko. Basic Concepts of X-ray Diffraction, 1st ed., Wiley VCH, Weinheim, 2014.

[24] N.S. Murthy, H. Minor, General procedure for evaluating amorphous scattering and crystallinity from X-ray diffraction scans of semicrystalline polymers, Polymer 31 (1990) 996–1002, https://doi.org/10.1016/0032-3861(90)90243-R.

[25] S.N. Ehrlich, J.C. Hanson, A. Lopez Camara, L. Barrio, M. Estrella, G. Zhou, R. Si, Combined XRD and XAS, Nucl. Instrum. Methods Phys. Res. A 649 (2010). OSTI ID: 1033214.

[26] C. Castellano, Combined approaches and challenges: XAS and X-ray diffraction, Int. Tables Cryst. Vol. I (2022), https://doi.org/10.1107/S1574870722001641.

[27] D. Lützenkirchen-Hecht, B. Bornmann, R. Frahm, P. Rothweiler, S. von Polheim, F. Eckelt, O. Müller, Simultaneous quick-scanning X-ray absorption spectroscopy and X-ray diffraction, J. Phys. Conf. Ser. 2380 (2022) 012130, https://doi.org/10.1088/1742-6596/2380/1/012130.

[28] P. Kotnik, P. Hofbauer, R. Resel, M. Koini, T. Haber, J. Keckes, DHS1100 - a new high temperature attachment for 4-circle X-ray goniometers, Acta Cryst. A62 (2006) s158, https://doi.org/10.1107/S010876730609684X.

[29] J. Keckes, J.W. Gerlach, R. Averbeck, H. Riechert, S. Bader, B. Hahn, H.-J. Lugauer, A. Lell, V. Härle, A. Wenzel, B. Rauschenbach, B, temperature dependence of stresses in GaN thin films grown on (0001) sapphire: modeling of thermal stresses, Appl. Phys. Lett. 79 (2001) 4307–4309, https://doi.org/10.1063/1.1427424.

[30] E. Eiper, R. Resel, C. Eisenmenger-Sittner, M. Hafok, J. Keckes, Thermally-induced stresses in thin aluminium layers grown on silicon, Adv. Xray Anal. 47 (2004) 368–372, https://doi.org/10.1154/1.1649326.

[31] W. Tillmann, L. Hagen, D. Kokalj, M. Paulus, M. Tolan, A study on the tribological behavior of Vanadium-Doped arc sprayed coatings, J. Therm. Spray. Tech. 26 (2017) 503–516, https://doi.org/10.1007/s11666-017-0524-y.

[32] C.A. Reiss, International Tables for Crystallography, H, IUCr, Chester, 2019, p. 153.

[33] S. Wannapaiboon, A. Schneemann, I. Hante, M. Tu, K. Epp, A.L. Semrau, C. Sternemann, M. Paulus, S.J. Baxter, G. Kieslich, R.A. Fischer, Control of structural flexibility of layered-pillared metal-organic frameworks anchored at surfaces, Nat. Commun. 10 (2019) 346, https://doi.org/10.1038/s41467-018-08285-5.

[34] D. Lützenkirchen-Hecht, B. Bornmann, R. Frahm, P. Rothweiler, S. von Polheim, F. Eckelt, O. Müller, Simultaneous quick scanning X-ray absorption spectroscopy and X-ray diffraction, J. Phys. Conf. Ser. 2380 (2022) 012130, https://doi.org/10.1088/1742-6596/2380/1/012130.

[35] F. Eckelt, P. Rothweiler, F. Braun, L. Voss, A. Šaric, M. Vrankic, D. Lützenkirchen-Hecht, In situ observation of ZnO nanoparticle formation by a combination of Time-Resolved X-ray absorption spectroscopy and X-ray diffraction, Materials 15 (2022) 8186, https://doi.org/10.3390/ma15228186.

[36] B. Bornmann, J. Kläs, O. Müller, D. Lützenkirchen-Hecht, R. Frahm, The quick EXAFS setup at beamline P64 at PETRA III for up to 200 spectra per second, AIP Conf. Proc. 2054 (2019) 040008, https://doi.org/10.1063/1.5084609.

[37] B. Ravel, M. Newville, ATHENA, ARTEMIS, HEPHAESTUS: data analysis for X-ray absorption spectroscopy using IFEFFIT, J. Synchrotron Rad. 12 (2005) 537–541, https://doi.org/10.1107/S0909049505012719.

[38] SpringerMaterials, Fe3P Crystal Structure, ⟨https://materials.springer.com/isp/crystallographic/docs/sd_0452183⟩, 2025 (accessed 13 March 2025).

[39] SpringerMaterials, Ni3P Crystal Structure, ⟨https://materials.springer.com/isp/crystallographic/docs/sd_0311218⟩, 2025 (accessed 06 April 2025).

[40] SpringerMaterials, Fe3B Crystal Structure, ⟨https://materials.springer.com/isp/crystallographic/docs/sd_0311376⟩, 2025 (accessed 09 April 2025).

[41] SpringerMaterials, Ni3B Crystal Structure, ⟨https://materials.springer.com/isp/crystallographic/docs/sd_0381984⟩, 2025 (accessed 01 May 2025).

[42] G. Ashiotis, Ashiotis, A. Deschildre, Z. Nawaz, J.P. Wright, D. Karkoulis, F. E. Piccac, J. Kieffer, The fast azimuthal integration python library: pyFAI, J. Appl. Crystallogr 48 (2015) 510–519, https://doi.org/10.1107/S1600576715004306.

[43] W. Kraus, G. Nolze, PowderCell for Windows Version 2.4, Federal Institute for Materials Research und Testing, Berlin (2000).

[44] P. Scherrer, Determining the size and internal structure of colloidal particles using X-rays (Transl.), Göttinger Nachr. Gesell 1918 (1918) 98. ⟨http://eudml.org/doc/59018⟩.

[45] A.L. Patterson, The scherrer formula for X-Ray particle size determination, Phys. Rev. 56 (1939) 978–982, https://doi.org/10.1103/PhysRev.56.978.

[46] P. Kizler, X-ray-absorption study of chemical short-range order in the amorphous Fe40Ni40P14B6 and Co70(Si,B)23Mn5(Fe,Mo)2 alloys, 47 (1993) 5660-5669. https://doi.org/10.1103/PhysRevB.47.5660.

[47] A. Paskin, T. Couasnon, J.P.H. Perez, S.S. Lobanov, R. Blukis, S. Reinsch, L. G. Benning, Nucleation and crystallization of ferrous phosphate hydrate via an amorphous intermediate, J. Am. Chem. Soc. 145 (2023) 15137–15151, https://doi.org/10.1021/jacs.3c01494.

[48] M. Neville, Fundamentals of XAFS, ⟨https://www.lehigh.edu/imi/teched/GlassCSC/SuppReading/Tutorials.pdf#:~:text=the%20chemical%20and%20physical%20state,for%20a%20selected%20atomic%20species⟩, 2004 (accessed 05 June 2025).

[49] E. Sevillano, H. Meuth, Extended x-ray absorption fine structure Debye-Waller factors. I. monatomic crystals, Phys. Rev. B 20 (1979) 4908, https://doi.org/10.1103/PhysRevB.20.4908.

[50] B. Opitek, J. Lelito, M. Szucki, G. Piwowarski, Ł. Gondek, Ł. Rogal, Analysis of the crystallization kinetics and thermal stability of the amorphous $Mg_{72}Zn_{24}Ca_4$ alloy, Materials 14 (2021) 3583, https://doi.org/10.3390/ma14133583.

[51] J. Huang, C. Jiang, Q. Wang, Influence of isothermal annealing on stress relaxation of shot peened SiCw/Al composite, ICSP-11, Conf. Proc. 2011 (2011) 2011046.

[52] J. Wang, Hc Kou, H. Chang, Xf Gu, Js Li, H. Zhong, L. Zhou, Limitation of the Johnson-Mehl-Avrami equation for the kinetic analysis of crystallization in a Ti-based amorphous alloy, Int J. Min. Met. Mater. 17 (2010) 307–311, https://doi.org/10.1007/s12613-010-0309-5.

[53] G. Williams, D.C. Watts, Non-Symmetrical dielectric relaxation behaviour arising from a simple empirical decay function, Trans. Faraday Soc. 66 (1970) 80–85, https://doi.org/10.1039/tf9706600080.

[54] J. Wu, X.Y. Chong, R. Zhou, Y.H. Jiang, J. Feng, Structure, stability, mechanical and electronic properties of Fe–P binary compounds by first-principles calculations, SC Adv. 5 (2015) 81943, https://doi.org/10.1039/c5ra09875k.

[55] A.B. Laursen, R.B. Wexler, M.J. Whitaker, E.J. Izett, K.U.D. Calvinho, S. Hwang, R. Rucker, H. Wang, J. Li, E. Garfunkel, M. Greenblatt, A.M. Rappe, G.C. Dismukes, Climbing the volcano of electrocatalytic activity while avoiding catalyst corrosion: Ni3P, a hydrogen evolution electrocatalyst stable in both acid and alkali, ACS Catal. 8 (2018) 4408–4419, https://doi.org/10.1021/acscatal.7b04466.

[56] M. Wang, A Program for Wavelet Transform of EXAFS Data from Athena, ⟨https://www.researchgate.net/publication/338644183_A_Program_for_Wavelet_Transform_of_EXAFS_Data_from_Athena⟩, (2019) https://doi.org/10.13140/RG.2.2.11521.61289/1 (accessed 25 June 2025).

[57] D. Lützenkirchen-Hecht, R. Wagner, S. Szillat, A.K. Hüsecken, K. Istomin, U. Pietsch, R. Frahm, The multi-purpose hard X-ray beamline BL10 at the DELTA storage ring, J. Synchrotron Radiat. 21 (2014) 819–826, https://doi.org/10.1107/S1600577514006705.

[58] S. Paripsa, L. Voss, F. Braun, F. Eckelt, D. Lützenkirchen-Hecht, Implementation of the quick-scanning EXAFS technique at DELTA beamline 10, J. Phys. Conf. Ser. 3010 (2025) 012076, https://doi.org/10.1088/1742-6596/3010/1/012076.
[59] A. Kuzmin, V. Dimitrijevs, I. Pudza, A. Kalinko, The use of the correlated debye model for extended X-Ray absorption fine Structure-Based thermometry in Body-Centered cubic and Face-Centered cubic metals, Phys. Status Solidi A (2024) 2400623, https://doi.org/10.1002/pssa.202400623.
[60] S. Paripsa, A. Gaur, F. Forste, D.E. Doronkin, W. Malzer, C. Schlesiger, B. Kanngiesser, E. Welter, J.-D. Grunwaldt, D. Lützenkirchen-Hecht, RefXAS: an open access database of X-ray absorption spectra, J. Synchrotron Rad. 31 (2024) 1105–1117, https://doi.org/10.1107/S1600577524006751.
[61] S. Paripsa, A. Gaur, F. Forste, D.E. Doronkin, W. Malzer, C. Schlesiger, B. Kanngiesser, E. Welter, J.-D. Grunwaldt, D. Lützenkirchen-Hecht, RefXAS: an open access database of X-ray absorption spectra – improvements and outlook, J. Phys. Conf. Ser. 3010 (2025) 012124, https://doi.org/10.1088/1742-6596/3010/1/012124.
[62] A. Gaur, S. Paripsa, F. Forste, D.E. Doronkin, W. Malzer, C. Schlesiger, B. Kanngiesser, E. Welter, J.-D. Grunwaldt, D. Lützenkirchen-Hecht, Metadata fields and quality criteria - XAS reference database under DAPHNE4NFDI, Proc. Conf. Res. Data Infrastr 1 (2023), https://doi.org/10.52825/cordi.v1i.258.